Computational Methods and Experimental Measurements XI, Ed. Brebbia, C.A., Carlomagno, G.M. and Anagnostopoulous, P. Halkidiki, Greece, May 2003.

Cartesian grid methods for simulating flows with moving boundaries

R. Mittal[1], C. Bonilla[2] & H.S. Udaykumar[3]
[1]*The George Washington University, USA*
[2]*University of Florida, USA*
[3]*University of Iowa, USA*

Abstract

A recently developed numerical method for flows with moving boundaries is used for simulating the flow-induced vibration of cylinders. The key feature of the numerical method is that it allows us to simulate flows with moving boundaries on stationary Cartesian grids. The key features of the method are described. The method is used to simulate (a) transverse flow-induced vibration of a cylinder in a freestream where the computed results are compared with theory and other simulations and (b) flow-induced vibration of a cylinder pair where we examine the effect of relative placement of the cylinders on the vibration of the two cylinders.

1 Introduction

In recent years there has been a surge of interest in numerical methods that compute flowfields with complex stationary and/or moving immersed boundaries on fixed Cartesian grids [1,2]. The obvious advantage of these methods over the conventional body-conformal approach is that irrespective of the geometric complexity of the immersed boundaries, the computational mesh remains unchanged. Cartesian grid methods free the underlying structured computational mesh from the task of adapting to the moving boundary, thus allowing large changes in the geometry due to boundary evolution. In the current paper, we apply a previously developed sharp-interface Cartesian grid solver [1,2] to two configurations with moving boundaries. The first is a canonical case of flow-induced vibration of a circular cylinder and the second involves the flow-induced vibration of a cylinder pair.

2 Numerical Method

The schematic in Figure 1 shows a solid with a curved boundary moving through a fluid, which illustrates the typical flow problem of interest here. The equations solved are the incompressible Navier-Stokes equations. The non-dimensionalized, integral form of these equations is given by:

$$\int_S \vec{u}\cdot\hat{n}\,dS = 0 \;; \qquad \mathrm{St}\frac{\partial}{\partial t}\int_V \vec{u}\,dV + \int_S \vec{u}(\vec{u}\cdot\hat{n})dS = -\int_S p\hat{n}\,dS + \frac{1}{\mathrm{Re}}\int_S \nabla\vec{u}\cdot\hat{n}\,dS \tag{1}$$

where $\vec{u}$ and p are the non-dimensional velocity and pressure respectively, St and Re are the Strouhal number and Reynolds number respectively which are defined as $\mathrm{St} = \omega L/U_o$ and $\mathrm{Re} = U_o L/\nu$, where ω is an imposed frequency, L the length scale, U_0 the velocity scale and ν the kinematic viscosity. In the above equations, subscript V and S denote the volume and surface of the control volume and $\hat{n}$ is a unit vector normal to the surface of the control volume. The above equations are to be solved with $\vec{u}(\vec{x},t) = \vec{u}_\partial(\vec{x},t)$ on the boundary of the flow domain where $\vec{u}_\partial(\vec{x},t)$ is the prescribed boundary velocity, including that at the moving immersed boundary. The above equations with the moving immersed boundary are to be discretized and solved on a Cartesian mesh shown in Figure 1.

A two-step, mixed explicit-implicit fractional step scheme [3] is used for advancing the solution of the above equations in time. The Navier-Stokes equations are discretized using a cell-centered, collocated (non-staggered) arrangement of the primitive variables ($\vec{u}$, p). In addition to the cell-center velocities which are denoted by $\vec{u}$, face-center velocities $\vec{U}$ are also computed. In a manner similar to a fully staggered arrangement, only the component normal to the cell-face is computed and stored (see Figure 1b). The face-center velocity is used for computing the volume flux from each cell in the current finite-volume discretization scheme. The advantage of separately computing the face-center velocities has been discussed in the context of the current method in Ye et al. [2]. The solution is advanced from time level t to $t+\Delta t$ through an intermediate advection-diffusion step where the momentum equations without the pressure gradient terms are first advanced in time. A second-order Adams-Bashforth scheme is employed for the convective terms and the diffusion terms are discretized using an implicit Crank-Nicolson scheme. This eliminates the viscous stability constraint, which can be quite severe in simulation of viscous flows. The discretized form of the advection-diffusion equation for each cell shown in Figure 1 can therefore be written as follows:

$$\mathrm{St}\frac{\vec{u}^{*}-\vec{u}^{t}}{\Delta t}\Delta V=-\frac{1}{2}\sum_{f}\left[3\vec{u}^{t}(\vec{U}^{t}\cdot\hat{n}_{f})-\vec{u}^{t-\Delta t}(\vec{U}^{t-\Delta t}\cdot\hat{n}_{f})\right]\Delta S_{f}$$
$$+\frac{1}{2\,\mathrm{Re}}\sum_{f}\left[\nabla u^{*}+\nabla u^{t}\right]\hat{n}_{f}\;\Delta S_{f} \tag{2}$$

where $\vec{u}^{*}$ is the intermediate cell-center velocity and subscript f denotes one face of the control volume. This equation is solved with the final velocity imposed as the boundary condition, i.e. $\vec{u}_{\partial}^{*}(\vec{x})=\vec{u}_{\partial}(\vec{x},t+\Delta t)$. The intermediate face-center velocities $\vec{U}^{*}$ are obtained at this point by interpolating the intermediate cell-center velocities $\vec{u}^{*}$. The advection-diffusion step is followed by the pressure-correction step in which the following integral equation is discretized:

$$St\int_{V}\frac{\vec{u}^{t+\Delta t}-\vec{u}^{*}}{\Delta t}dV=-\int_{V}\nabla p^{t+\Delta t}dV \tag{3}$$

By requiring a divergence-free velocity field at the end of the time-step the following elliptic equation for pressure is obtained:

$$\sum_{f}\nabla p^{t+\Delta t}\cdot\hat{n}_{f}\;\Delta S_{f}=\frac{\mathrm{St}}{\Delta t}\sum_{f}\vec{U}^{*}\cdot\hat{n}_{f}\;\Delta S_{f} \tag{4}$$

With stationary, non-porous boundaries, a homogeneous Neumann boundary condition for pressure results in a consistent approximation of the Navier-Stokes equations [4]. Once the pressure is obtained by solving Eq. (4), both the cell-center and face-center velocities, $\vec{u}$ and $\vec{U}$ are updated separately as follows:

$$\vec{u}^{t+\Delta t}=\vec{u}^{t}-\Delta t(\nabla p^{t+\Delta t})_{cc}\,;\qquad \vec{U}^{t+\Delta t}=\vec{U}^{t}-\Delta t(\nabla p^{t+\Delta t})_{fc} \tag{5}$$

where subscripts *cc* and *fc* indicate evaluation at the cell center and face center locations respectively. Further discussion regarding the adoption of cell-center and face-center velocities can be found in Zang et al [5] and in the context of the present method in Ye et al. [2].

The key element in the finite-volume discretization of the Eqs. (2)-(4) in the context of the current method is the evaluation of fluxes and derivatives at the faces of each control volume. These include momentum, mass and diffusive fluxes and gradients of pressure. A detailed discussion of this aspect, including validation of the accuracy of the solution procedure has been presented in Ye et al. [2] and Udaykumar et al. [3]. In the rest of the paper, we focus on the application of this method to three problems with moving boundaries.

3 Simulation Results

3.1. Flow-Induced Vibration of a Cylinder

This is a canonical flow configuration that is often used to validate the accuracy of numerical solvers. In these simulations the cylinder is allowed to vibrate naturally in the vertical (transverse) direction in response to unsteady hydrodynamic forces.

$$\frac{2m}{\rho D^2}\ddot{y}^* + \frac{2C}{\rho U_\infty D}\dot{y}^* + \frac{2k}{\rho U_\infty{}^2} y^* = C_L(t^*) \qquad (6)$$

where m is the mass of the system per length of the cylinder, C is the damping constant per length of the cylinder and k is the spring constant per length of the cylinder. C_L is the coefficients of lift which is a periodic (or quasiperiodic) function with a characteristic frequency equal to the vortex shedding frequency ω_s. Furthermore, ρ is the density of the fluid, U_∞ is the velocity of the fluid and D is the diameter of the cylinder.

We also define ω_n^* and ω_s^* as the non-dimensional natural frequency and the non-dimensional shedding frequency, which is equivalent to the Strouhal number (S_t).

$$\omega_n = \frac{\omega_n^* U_\infty}{D}; \qquad \omega_s = \frac{\omega_s^* U_\infty}{D} = \frac{2\pi S_t U_\infty}{D} \qquad (2.8b)$$

From equation (6) the non-dimensional mass, damping and stiffness are obtained as

$$m^* = \frac{2m}{\rho D^2} = \frac{\pi}{2}\frac{\rho_s}{\rho}\,;\; C^* = \frac{2C}{\rho U_\infty D} = \frac{4m\zeta\omega_n}{\rho U_\infty D} \text{ and } k^* = \frac{2k}{\rho U_\infty{}^2} = \omega_n^{*2}\left(\frac{\pi\rho_s}{2\rho} + \frac{\pi}{2}\right)$$

where ρ_s is the density of the cylinder per length, ω_n is the natural frequency and ζ is the system damping ratio. It should also be noted that the natural frequency is not determined by the system mass but instead by the combined system mass and added mass. The equation of motion of the cylinder is discretized and solved in a loosely coupled manner with the flow equations and the flow is simulated at a Reynolds number of 200 and cylinder mass m^* is set to 10.0.

First we present results showing the variation of the vibration amplitude with reduced damping which is denoted as $S_g = \pi\beta/4$ where $\beta = C^*\omega_s^* = 2\pi S_t C^*$. Figure 2 shows the typical non-uniform Cartesian grid used for the simulations. In this grid, extra resolution is provided in the vicinity of the cylinder and in the wake. Figure 3 shows spanwise vorticity contour plots and transverse cylinder displacement for two representative cases which clearly show the extent of the cylinder vibration and the effect of the vibration on the vortex shedding from the cylinder. Simulations have been carried out for a wide range of values of the reduced damping parameter and in figure 4 we compare our results against the phenomenological model of Blevins et al. [6] and Blevins [7] as well as the simulations of Blackburn and Karniadakis [8]. It can be seen that our results compare quite well with the latter and the trend matches that predicted by theory. This provides strong validation of the overall computational methodology.

3.2. Flow-Induced Vibration of a Cylinder Pair

The study of the flow induced vibration of a cylinder pair is essential in many areas of engineering. Most of the studies to date have focused on the vibration of a single cylinder. However, the vibration of a pair of cylinders in close proximity is expected to be significantly different from that of a single isolated cylinder. Applications where the vibration of a cylinder pair would be of interest include (a) tubular heat exchangers, (b) marine risers (c) marine support structures (d) smokestacks (e) antennas (f) tall skyscrapers and (g) fibers during processing. Most previous studies of this configuration have been experiments [9,10]. Here we use numerical simulations to explore the flow-induced vibration of a cylinder pair.

The simulations described in this chapter are meant to highlight the effects of flow coupling on two identical but otherwise independent cylinders. The simulations are meant to explore the effect of the flow on cylinders positioned in-line, perpendicular, as well as oblique to the flow. The simulations will also examine the effect that the cylinder spacing has on the vibration of the cylinders.

The cylinder mass is set to m^*=10.0 and Re=200. The cylinder parameters are such that both β=0.03 and U^*=4 for all cases. A total of nine simulations have been conducted and compared with a single elastic cylinder as well as with each other. The tested parameters are cylinder separation and arrangement configuration. The separation is non-dimensionalized by the cylinder diameter and is measured from cylinder center to center. $d^* = d / D$, where d is the cylinder separation distance from surface to surface and D is the cylinder diameter. The values of d^* for the experiments is 1, 2 and 3 as shown in figure 4.2. The cylinders are arranged in 3 configurations for each distance. The value of θ for the experiments is 0°, 45° and 90° as is shown in figure 5. Typical grid for these simulations employs 282x262 grid points.

Figure 6 shows vorticity contour plots for two cases where the cylinders are placed in an inline arrangement. Figure 7 shows the cylinder displacement for these two cases. It can be seen that when the distance between the two cylinders in this arrangement is small, the vortex shedding from the upstream cylinder is suppresses and furthermore, the vortex shedding behind the downstream cylinder occurs much further downstream of the cylinder than in the case of a single cylinder. This results in the suppression of vibration in both cylinders. However, as the distance is increased, vortex shedding behind the upstream cylinders resumes and this results in a larger amplitude vibration of both cylinder.

Figure 8 shows results for two cases where the cylinders are not inline and it can be seen that the vortex shedding is quite different for these configuration. Finally, Figure 9 summarizes the results of all the calculation carried out for the cylinder pair configuration. A comparison with respect to reduced distance shows different trends for the leading and trailing cylinders. The leading cylinders have a tendency to increase in RMS amplitude as the distance increases, as if the trailing cylinder served as a damper. This is not the case for the 90° configuration where there is no such thing as a leading and trailing cylinder. The trailing cylinder decreased for the 45° case but increased for the 0° case. A comparison with respect to θ shows little dependence to θ for a reduced distance of 2, and a large dependence to θ for a reduced distance of 1. Aside from the case where θ=0°the values of d^*=3 showed little dependence to θ. However at θ=0° the value of d^*=3 gave one of the largest response and the largest rate of change.

4 Summary

The simulations presented here demonstrate the ease with which Cartesian grid methods can be used to simulate relatively complex fluid-structure interaction problems. It should be noted that these all simulations reported here have been performed on desktop UNIX and LINUX workstations and in most cases, require at most on the order of ten hours of CPU time. The Cartesian grid methodology has also been extended to three-dimensional incompressible and compressible flows and these results will be presented elsewhere.

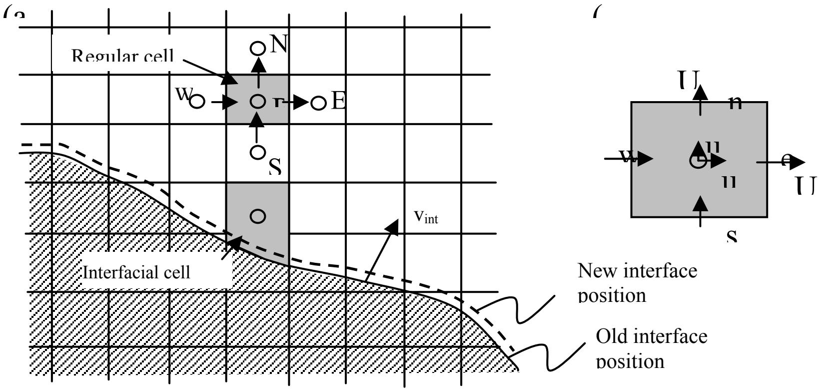

Figure 1. (a) Illustration of a moving boundary cutting through a fixed mesh. Cells traversed by the interface are called interfacial cells. Cells away from the interface are regular cells. (b) A regular cell

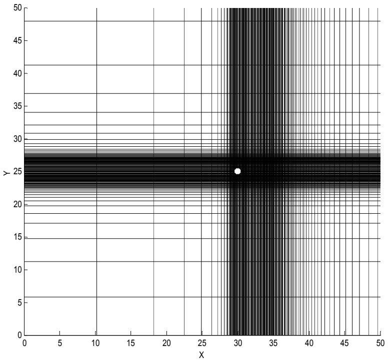

Figure 2. Non-uniform grid used for numerical analysis in the Cartesian Grid code. Only every other gridline is shown in both directions.

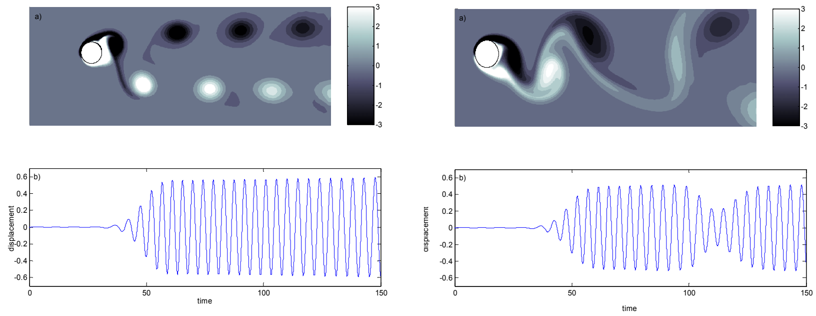

(a) (b)

Figure 3. Contour plot of vorticity and transverse displacement of cylinder as a function of time (a) β=0.003. (b) β=0.3

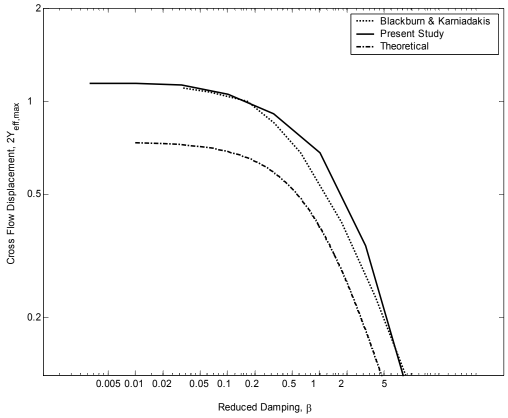

Figure 4. Comparison of mean values of peak-to-peak free vibration oscillation amplitudes as a function of reduced damping with Refs. [6] and [7].

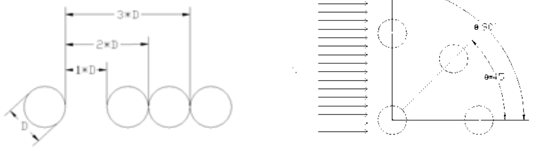

Figure 5. (a) The value of d^* ranges from 1 to 3. The value of the diameter (D) for all the cases is 1. (b) The value of θ ranges from 0°to 90.

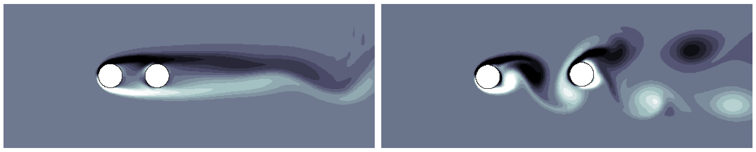

Figure 6. Contour plot of vorticity for the case of (a) d^*=1 and θ=0. (b) d^*=3 and θ=0

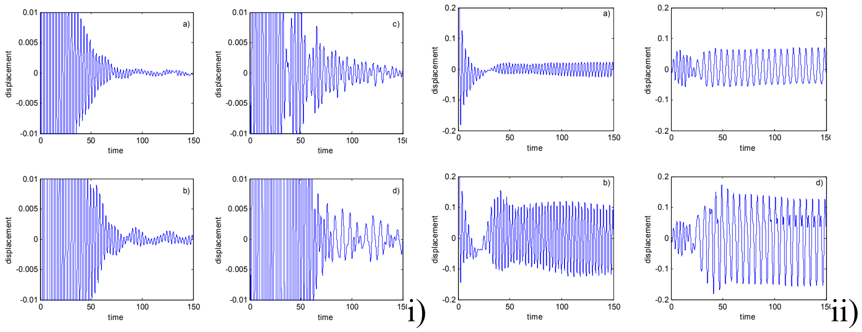

Figure 7. Cylinder displacement as a function of time for (i) d^*=1 and θ=0. (ii) d^*=3 and θ=0 (a) x-displacement of leading cylinder. (b) x-displacement of trailing cylinder. (c) y-displacement of leading cylinder. (d) y-displacement of trailing cylinder.

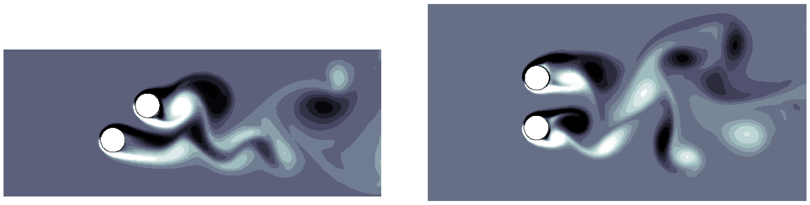

(a) (b)

Figure 8. Spanwise vorticity contours and (a) d^*=1 and θ=45°.. (b) d^*=3 and θ=90° For each case:

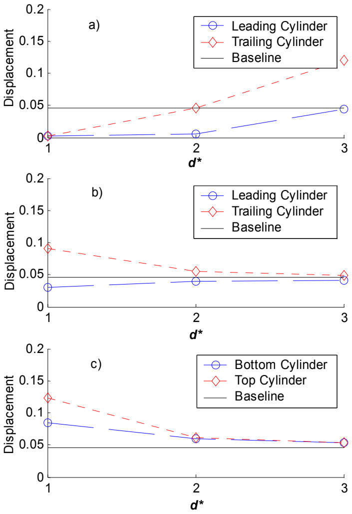

Figure 9. Cylinder response (absolute RMS displacement) as a function of d^*.for the cylinder pair a) θ=0. b) θ=45°. c) θ=90°

References

[1] Udaykumar, H. S., Mittal, R., and Shyy, W. 1999. Solid-Liquid Phase Front Computations in the Sharp Interface Limit on Fixed Grids. *J. Comp Phys.,* Vol. 18, pp. 535-574.

[2] Ye, T., Mittal, R., Udaykumar, H. S. and Shyy, W. 1999. An Accurate Cartesian Grid Method for Viscous Incompressible Flows with Complex Immersed Boundaries, *J. Comp. Phys.* Vol. 156, pp. 209-240.

[3] Chorin, A. J. “Numerical solution of the Navier-Stokes equations,” *Math. Comput.* 22, 745 (1968).

[4] Temam R. "Remarks on the Pressure Boundary Condition for the Projection Method." *Theor. Comput. Fluid Dyn*. 3, 181-184, 1991.

[5] Zang, Y. Street R. L. and Koseff, J. R., “A non-staggered grid, fractional step method for time-dependent incompressible Navier-Stokes equations in Curvilinear coordinates,” *J. Comput. Phys*. 114, 18 (1994).

[6] Blevins, R. D. 1990. Flow-Induced Vibration, 2nd ed. New York: Van Nostrand Reinhold.

[7] Blevins, R. D., and Burton, T. E. 1976. Fluid Forces Induced by Vortex Shedding. *Journal of Fluids Engineering – Transactions of the ASME,* Vol. 98(1), pp. 19-26.

[8] Blackburn, H. M., and Karniadakis, G. E. 1993. Two and Three Dimensional Simulations of Vortex-Induced Vibration of a Circular Cylinder. Third International Offshore and Polar Engineering Conference, Vol. 3, pp. 715-720, Singapore

[9] Jendrzejczyk, J. A., Chen, S. S., and Wambsganss, M. W. 1979. Dynamic Response of a Pair of Circular Tubes Subjected to Liquid Cross Flow. *Journal of Sound and Vibration.* Vol. 67, pp. 263-273.

[10] King, R., and Johns D. J. 1976. Wake Interaction Experiments With Two Flexible Circular Cylinders in Flowing Water. *Journal of Sound and Vibration.* Vol. 45, pp. 259-283.